

Incoherent synchrotron emission of laser-driven plasma edge

D. A. Serebryakov,^{1,2,a)} E. N. Nerush,^{1,2} and I. Yu. Kostyukov^{1,2}

¹⁾*Institute of Applied Physics of the Russian Academy of Sciences, 46 Ulyanov St., Nizhny Novgorod 603950, Russia*

²⁾*Nizhny Novgorod State University, 23 Gagarin Avenue, Nizhny Novgorod 603950, Russia*

(Dated: 25 August 2015)

When a relativistically intense linearly polarized laser pulse is incident on an overdense plasma, a dense electron layer is formed on the plasma edge which relativistic motion results in high harmonic generation, ion acceleration and incoherent synchrotron emission of gamma-photons. Here we present a self-consistent analytical model that describes the edge motion and apply it to the problem of incoherent synchrotron emission by ultrarelativistic plasma electrons. The model takes into account both coherent radiation reaction from high harmonics and incoherent radiation reaction in the Landau-Lifshitz form. The analytical results are in agreement with 3D particle-in-cell simulations in a certain parameter region that corresponds to the relativistic electronic spring interaction regime.

I. INTRODUCTION

Gamma-rays and hard X-rays have become widely applied since their discovery. Most of present-day gamma-ray sources are based on the radioactive decay, bremsstrahlung, and backward Compton scattering; however, one needs to deal with radioactive materials or large-scale electron accelerators (linacs or synchrotrons) to use them and it limits their availability. The growing demand for gamma-ray sources in numerous fields (medicine, radiography, nuclear physics) drives search for more convenient and accessible sources of hard X-rays and gamma-rays. In the recent decades an outstanding progress in laser technologies has been achieved, and now high-power (> 100 TW) short-pulse lasers have become commercially available. Due to ultrahigh electromagnetic fields that they produce, lasers may be used to improve brightness and flux of gamma-ray sources. Namely, laser wake field acceleration (LWFA) is used to produce high-charge electron bunches for bremsstrahlung^{1,2} and Compton sources^{3–7}; some other techniques are also proposed^{8–10}, one of them is incoherent synchrotron emission of plasmas lit by high-power laser pulses.

When a relativistically intense laser pulse interacts with a target, the target electrons are expelled from atoms and accelerated to relativistic speeds, then the laser field forces them to emit photons due to Compton scattering. If the laser field amplitude E_0 is such that $a_0 \equiv eE_0/mc\omega \ggg 1$ (where c is the speed of light, ω is the laser field angular frequency, m and $e > 0$ are the electron mass and charge, respectively), the spectrum of emitted photons becomes synchrotron-like with a tail up to MeV or above. Earlier estimations and numerical simulations show that a large fraction of the laser pulse energy may be transformed into gamma-rays if laser intensity is high enough, e.g. percents^{11–13} for $I \gtrsim 10^{22} \text{ W cm}^{-2}$ and tens of percent^{14–16}

for $I \gtrsim 10^{24} \text{ W cm}^{-2}$, so such gamma-ray sources look very promising (compared to linear Compton scattering-based sources with lower conversion efficiency, and to relatively complicated LWFA sources). But these phenomena are commonly studied by particle-in-cell codes, and currently a few analytical models are proposed.

In this paper we present a self-consistent analytical model describing nonlinear electron motion in a thin dense layer arising at a laser-irradiated plasma edge in a specific parameter region. The corresponding laser-plasma interaction regime is referred as the *relativistic electronic spring*¹⁷ (RES), and is mostly considered in the context of attosecond pulse generation^{17,18}. In the RES regime a sizable portion of the laser energy is transferred into electron oscillations¹⁷ that seems preferable for efficient photon emission. The thickness of the electron layer in the RES regime may be as small as 1 nm, which makes coherent synchrotron emission feasible^{17–19}. The wavelength of 1 nm approximately corresponds to the photon energy of 1 keV, therefore higher photon energies can be obtained only by the *incoherent synchrotron emission* (ISE). However, for laser intensities $I \gtrsim 10^{22} \text{ W cm}^{-2}$ average photon energies of single electron synchrotron spectrum are far beyond the limit of coherent emission; that's why ISE can be very efficient. We compute radiation pattern and other properties of ISE in RES regime using the proposed analytical model for the plasma edge dynamics.

Analytical results are verified by 3D particle-in-cell (PIC) simulations that take into account photon emission with radiation reaction and electron-positron pair production from hard photons¹³. Despite PIC simulations reveal more complicated electron dynamics than assumed in the model, the model describes well the plasma edge motion and the gamma-ray radiation pattern in a certain parameter region. Numerical simulations also allow us to distinguish various laser-plasma interaction regimes and compare gamma-ray generation efficiency between them.

^{a)}Electronic mail: dmserebr@gmail.com

II. ANALYTICAL MODEL FORMULATION

To describe collective electron dynamics and hard photon emission, let us introduce a self-consistent model of electron layer movement. Several major assumptions are pointed out. First, under the light pressure electrons of the irradiated plasma edge form a very thin layer (in comparison with the laser wavelength) which moves in such a way that laser pulse reflects from the target almost completely, so we can neglect electron density perturbations behind the layer. Second, we consider normal incidence of linearly polarized laser pulses and assume that the layer electrons move in the polarization plane. Third, only collective electron dynamics is considered (we suppose that the dispersion of individual electron characteristics inside the layer does not affect hard photon emission drastically and just results in a smoothing of the radiation pattern, photon spectrum, etc). The last assumption is that the ion motion is neglected: we restrict ourselves to the case of few-cycle laser pulses so that the interaction time is short enough, or to the case of quite low laser intensity so that the ion displacement is negligible.

The total force driving the layer electrons consists of the following parts: force caused by the incident laser field, force from self-generated electromagnetic fields (i.e. fields coherently emitted by the layer), force caused by electron-ion separation and radiation reaction force (i.e. force caused by ISE). Unlike the model of Ref. 17, we do not adopt the requirement that the laser field behind the layer is completely compensated by the self-generated fields: this requirement makes it impossible to obtain Lorentz factor of the electrons^{13,17}. Instead, we start from the equations of motion that takes into account all the force parts mentioned above:

$$\frac{dp_x}{dt} = -E_x - v_y B_z + F_{rx}, \quad (1)$$

$$\frac{dp_y}{dt} = -E_y + v_x B_z + F_{ry}, \quad (2)$$

$$\mathbf{E} = \mathbf{E}_l + \mathbf{E}_p, \quad (3)$$

$$\mathbf{B} = \mathbf{B}_l + \mathbf{B}_p, \quad (4)$$

where \mathbf{p} is the electron momentum normalized to mc , \mathbf{v} is the electron velocity normalized to c , \mathbf{E} and \mathbf{B} are the electric and magnetic fields, respectively, normalized to $mc\omega/e$, indexes l and p denote laser and plasma fields (plasma fields are coherent emission and charge separation fields), and \mathbf{F}_r is the radiation reaction force (caused by ISE). Here we assume that the laser pulse is incident along x axis and the polarization plane is the xy plane.

The models similar to Eqs. (1)-(4) have been described in Refs. 20 and 21. They account only the radiation reaction caused by the fields coherently emitted by the layer, i.e., transverse components of E_p and B_p . On the contrary, this model considers both the coherent part of radiation reaction (from coherent high harmonics emission) and the radiation reaction force caused by the incoherent emission of high-frequency photons. The wavelengths

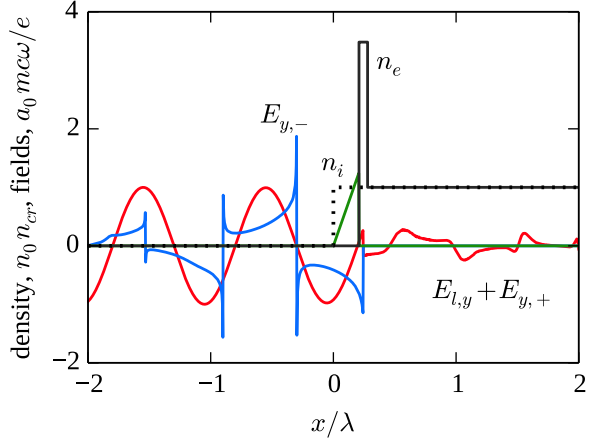


FIG. 1. Schematic structure of the electron layer at the plasma edge and fields in RES regime. Curves: electron density, gray; ion density, black dotted; E_x , green; sum of the laser field and the field emitted by the layer in $+x$ direction ($E_{l,y} + E_{y,+}$), red; the wave emitted by the layer in $-x$ direction ($E_{y,-}$), blue.

of these photons (emitted by single electrons) are much smaller than the layer thickness so they cannot be coherently summarized.

As stated above, we consider the incidence of a laser pulse on a plasma half-space (unlike Ref. 21 considering a foil much thinner than the laser wavelength). Therefore, the areal charge density of the layer is a function of the layer position, and according to RES assumption¹⁷ is the following:

$$\epsilon = n_0 x_\ell, \quad (5)$$

where the charge density is normalized to cn_{cr}/ω , n_0 is the initial electron density normalized to the critical plasma density $n_{cr} = m\omega^2/4\pi e^2$, x_ℓ is the layer displacement from the initial plasma edge position normalized to $\lambda/2\pi = c/\omega$. The fields coherently emitted by the layer can be then easily found from the Maxwell's equations^{13,17,18}:

$$E_{y,+} = B_{z,+} = \frac{\epsilon v_y}{2(1-v_x)}, \quad (6)$$

$$E_{y,-} = -B_{z,-} = \frac{\epsilon v_y}{2(1+v_x)}, \quad (7)$$

$$E_x = \frac{\epsilon x}{x_\ell} \text{ if } 0 < x < x_\ell, \quad (8)$$

where indices $+$ and $-$ denote field values at $x_\ell \pm 0$ and also denote waves emitted by the layer in $+x$ and $-x$ directions. E_x can be found as a flat capacitor field since the ions are immobile. An example of the fields generated by the electron layer oscillating according to Eqs. (10)-(13) (see below) is shown in Fig. 1.

The radiation reaction force caused by ISE may become significant at field intensities of $\gtrsim 10^{21}-10^{22} \text{ W/cm}^2$

so it shouldn't be neglected for the sake of consistency^{22–25}. The main term in Landau-Lifshitz approximation of the radiation reaction force is the following²⁶:

$$\mathbf{F}_r = -\frac{4\pi}{3} \frac{r_e}{\lambda} \left[(\gamma \mathbf{E} + \mathbf{p} \times \mathbf{B})^2 - (\mathbf{p} \cdot \mathbf{E})^2 \right] \mathbf{v}, \quad (9)$$

where $r_e = e^2/mc^2$ is the classical electron radius and $\gamma = \sqrt{1+p^2}$ is the electron Lorentz factor. The radiation reaction efficiently decelerates the emitting electrons and modifies their movement, however, we observe that the trajectory doesn't change qualitatively. Anyway, the Lorentz factor and its distribution along the electron trajectory is affected by the radiation reaction that can yield modification of total power and radiation pattern of the emitted gamma-rays.

It can be easily estimated from Eq. (9) that for a simple circular trajectory in rotating electric field radiation reaction force is equal to the Lorentz force when the dimensionless field magnitude reaches $a_{thr} = \sqrt[3]{3\lambda/4\pi r_e} \approx 400$ for optical wavelengths. For more complex trajectories radiation reaction force can be higher than for circular trajectory. Anyway, for more strict consideration radiation reaction force should be taken into account if $a_0 \gtrsim 100 - 400$.

Since a field affecting the layer can be found as a half-sum of fields on both layer sides, the system of equations that governs collective electron dynamics turns to be

$$\frac{dp_x}{dt} = -\frac{n_0 x_\ell}{2} \left(1 + \frac{v_x v_y^2}{1 - v_x^2} \right) - v_y E_{ly} + F_{rx}, \quad (10)$$

$$\frac{dp_y}{dt} = -\frac{n_0 x_\ell v_y}{2} - (1 - v_x) E_{ly} + F_{ry}, \quad (11)$$

$$\frac{dx_\ell}{dt} = v_x = \frac{p_x}{\gamma_\ell}, \quad (12)$$

$$\frac{dy_\ell}{dt} = v_y = \frac{p_y}{\gamma_\ell}. \quad (13)$$

A. Some model properties

In this subsection we neglect radiation reaction force \mathbf{F}_r in order to demonstrate clearly a number of results of the model. First, the equation for Lorentz factor can be found from Eqs. (10)-(13) and is the following:

$$\frac{d\gamma_\ell}{dt} = -(E_{ly} + E_{y,+}) v_y - \frac{n_0 x_\ell v_x}{2(1 + v_y^2 \gamma_\ell^2)}. \quad (14)$$

Thus, the electron Lorentz factor is determined by the field transmitted through the layer, $E_{ly} + E_{y,+}$, and by the effective longitudinal field reduced by a factor of $1 + v_y^2 \gamma_\ell^2$. Lets assume that $\gamma_\ell \gg 1$ and $|E_{ly} + E_{y,+}| \ll a_0$, hence $d\gamma/dt \ll dp_x/dt$. In this case Eqs. (10) and (11) together with $d(v_x^2 + v_y^2)/dt \approx 0$ yield: $v_y E_{ly} + n_0 x_\ell (1 + v_x)/2 \approx 0$. This equation is equivalent to the following: $E_{ly} + E_{y,+} \approx 0$.

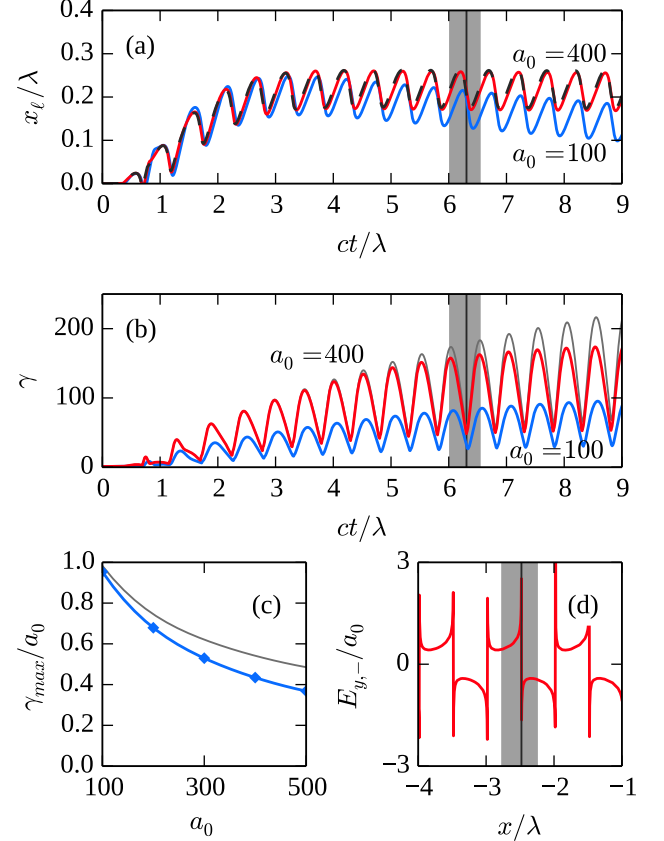


FIG. 2. (a) The layer position given by the model for $a_0 = n_0 = 400$ (red curve) and $a_0 = n_0 = 100$ (blue curve). The dashed black curve corresponds to the layer motion that yields a complete compensation of the incident field behind the layer¹³ for $n_0 = a_0$. (b) The Lorentz factor of the above-mentioned trajectories. Thin grey curve corresponds to Eqs. (10)-(13) with \mathbf{F}_r neglected, $a_0 = n_0 = 400$. (c) Maximal Lorentz factor gained by the layer electrons for $a_0 = n_0$ at 9 periods of the incident field vs the incident field magnitude according to the analytical model (blue curve with markers), and the same with \mathbf{F}_r neglected (thin grey curve). (d) The field reflected by the layer, $a_0 = n_0 = 400$, at $t = 9\lambda/c$. The gray area denotes a trajectory half period bounded by $v_x \approx 1$ points, vertical dark grey line denotes a time instant where $v_x \approx -1$.

Therefore, Eqs. (10)-(13) lead to the layer dynamics that almost completely compensates the incident field behind itself. This means that the trajectory obtained from the model is close to the layer trajectory obtained in the framework of Refs. 13 and 17 in which the layer trajectory is found from the strict requirement $E_{ly} + E_{y,+} = 0$, that can be rewritten as follows¹³:

$$\frac{dx_\ell}{dt} = \frac{4E_{ly}^2 - n_0 x_\ell^2}{4E_{ly}^2 + n_0 x_\ell^2}. \quad (15)$$

However, the latter model assumes that Lorentz-factor is constant along the layer trajectory and doesn't allow to find the radiation pattern since it highly depends on γ

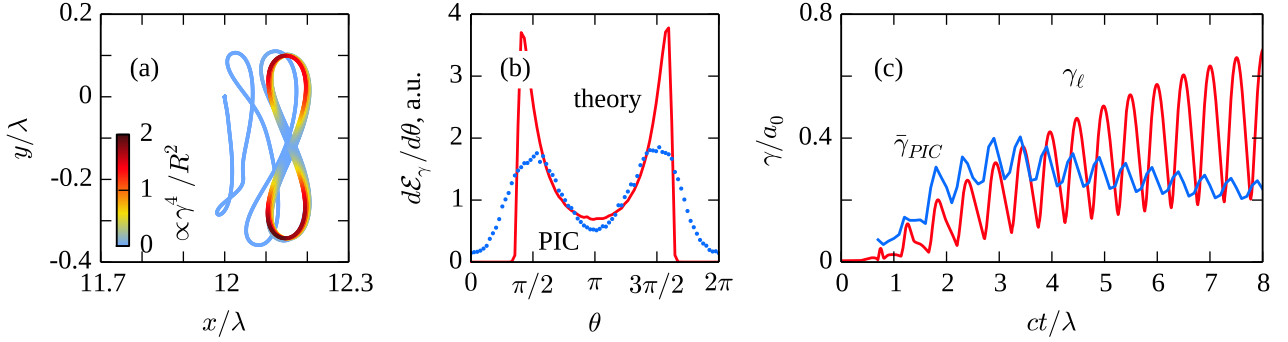


FIG. 3. (a) The layer trajectory for $a_0 = 240$ and $n_0 = 320$ obtained from Eqs. (10)-(13), color corresponds to γ^4/R^2 . (b) Radiation pattern for the theory (solid) and PIC (dotted); ϑ is the angle in the polarization plane, $\vartheta = 0$ corresponds to the direction of x axis. (c) Lorentz factor in the model γ_ℓ , and the average Lorentz factor $\bar{\gamma}_{PIC}$ of electrons with $\gamma > 0.05a_0$.

distribution along the trajectory.

Since the terms of Eq. (14) may be of the same order and the last term should not be neglected, a_0 cannot be excluded from Eqs. (10)-(13) by a normalization, and not the only parameter n_0/a_0 governs the layer dynamics, but both a_0 and n_0 . This means that the scaling law proposed in Refs. 13, 17, and 27 can be invalid for laser-plasma interactions in RES regime.

The described model properties are illustrated in Fig. 2 where numerical solution of Eqs. (10)-(13) is shown. First, it is seen that x_ℓ given by the model of the present paper is close to the layer position given by models of Refs. 13 and 17. Second, due to the field compensation γ_ℓ increases with time quite slowly and even for several laser periods γ_ℓ/a_0 remains $\lesssim 1$. Furthermore, γ_ℓ/a_0 drops with the instantaneous increase of a_0 and n_0 . Third, radiation reaction doesn't change the interaction picture considerably.

B. ISE in the model

Eqs. (10)-(13) don't allow analytical solution and should be solved numerically. Solution depends on the parameters a_0 , n_0 and laser pulse shape.

The sample electron layer trajectory for typical modeling parameters is shown in Fig. 3(a). The asymptotic trajectory resembles number 8 and is similar to a particle trajectory in a linear-polarized EM wave (for a free particle it looks like number 8 only in a proper reference frame, though). For $a_0 = 240$ the maximum value of Lorentz factor is 120 and corresponds to the middle part of trajectory (where curve intersects itself); the minimum γ value is in the order of ten. The distribution of the layer energy over the trajectory yields the electron layer radiation pattern. Given that energy is ultrarelativistic over the whole period ($\gamma \gg 1$), radiation mechanism is almost purely synchrotron — practically all gamma quanta are emitted in the tangential direction. So we can use the following formula for the emission power of a single electron

at each instant of time:

$$I_e = \frac{2e^2 c \gamma^4}{3R^2} \quad (16)$$

where R is the curvature radius of the trajectory at the current point. For gamma quanta emitted by the whole layer we get

$$I_{layer} \sim \frac{\gamma^4}{R^2} X_l \quad (17)$$

On-axis distribution of the hard photon density is shown in Fig. 4(a), and the radiation pattern is shown in Fig. 3(b). On the curved part of the trajectory the gamma-rays are generated most efficiently due to small curvature radius, but the radiation direction changes rapidly at this point. It's the central part of the trajectory that mostly contributes into the radiation pattern.

The gamma ray radiation pattern shown in Fig 3(b) corresponds to the trajectory from Fig. 3(a). The dotted line is the pattern that was produced by PIC 3D numerical simulations (see Sec. III for details). The pattern has two lobes in the plane of the laser \mathbf{E} and \mathbf{k} vectors. Lobes position depends on the laser pulse intensity; with greater intensity, the maximums are closer to the x -direction. In this model, nothing is emitted strictly forward because the layer electrons are never moving exactly in the $+x$ direction. Qualitatively the model and numerical results are in agreement with each other, however simulations don't give sharp peaks in the radiation pattern due to electron velocity spread which is neglected in model.

III. RESULTS OF NUMERICAL SIMULATIONS

In order to validate the model results, we have performed a series of numerical PIC simulations. The code used for is fully three-dimensional and can take into account the quantum electrodynamical (QED) effects¹³. The code supports parallelization so it can be efficiently used on computational clusters.

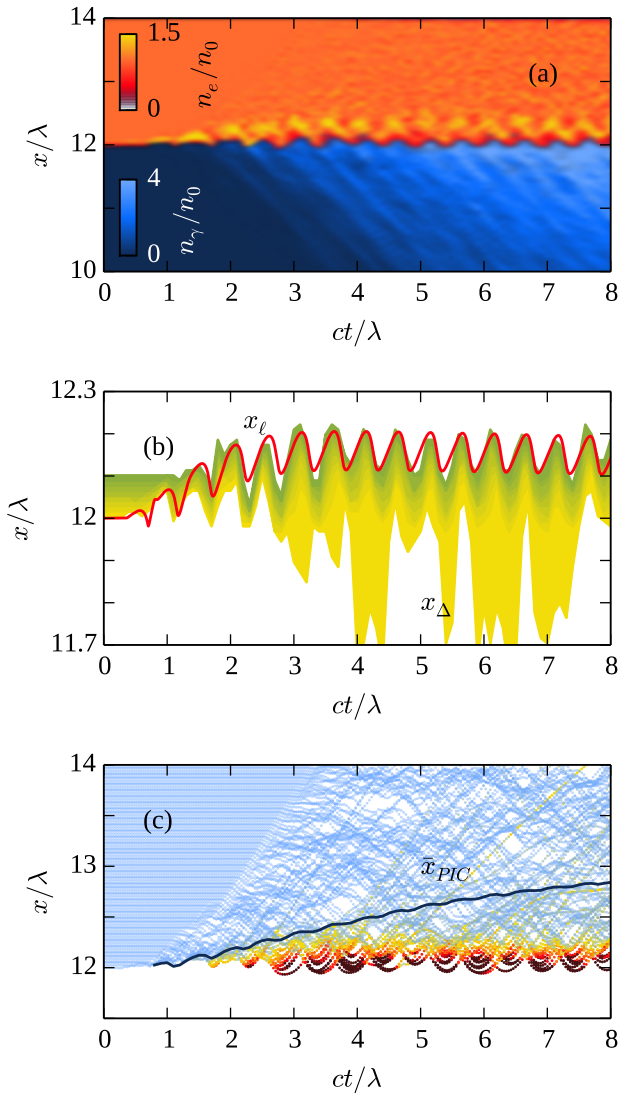


FIG. 4. (a) On-axis electron and photon densities obtained in PIC for $a_0 = 240$ and $n_0 = 320$. (b) For the same parameters, the analytical trajectory (red) and x_Δ according to Eq. (19) for $\Delta = 0.01\lambda$ (lower boundary) and $\Delta = 0.11\lambda$ (upper boundary). (c) Tracks of individual electrons obtained in PIC simulation. The color intensity corresponds to γ^4/R^2 . The average trajectory of the electrons with $\gamma > 0.05a_0$, \bar{x}_{PIC} .

We have simulated the interaction of a falling $1\text{ }\mu\text{m}$ wavelength linear-polarized laser pulse with a flat $2\text{ }\mu\text{m}$ wavelength foil. The laser pulse intensity and foil density varied between different PIC runs. In this series, we considered the ions as fixed; conditions of applicability of this assumption are discussed in the section IV. Laser pulse envelope has the following shape:

$$E_y(x) = \frac{d}{dx} \left\{ \sin x \cos^2 \left(\frac{\pi(x+x_s)^4}{2x_s^4} \right) \right\} \quad (18)$$

It corresponds to a wavepacket which has almost constant amplitude in the central area and promptly decreases at

the x_s distance from the pulse center. Therefore the configuration becomes much close to idealized modeling situation (falling of a plain wave onto a flat target).

A. Electron layer dynamics

In a certain region of simulation parameters a layer with high electron density is formed in the front side of the target (see Sec. IV for details). Its thickness is in the order of 100 nm . Due to $\mathbf{v} \times \mathbf{B}$ force caused by linearly polarized laser pulse the plasma edge is oscillating in the direction of pulse propagation (see Fig. 4(a)). Electrostatic force caused by the ions compensates the light pressure on the average and holds the layer.

From the numerical simulations we can acquire the layer trajectory and compare it to the analytical one. Current position x_Δ of the layer in PIC is calculated using the following formula

$$\Delta = \int_{-\infty}^{x_\Delta} n_e(x)/n_{cr} dx, \quad (19)$$

where Δ is some given in advance number of electrons. If the electrons form a thin layer and Δ is less than a number of electrons in the layer, x_Δ is approximately equal to the layer position for any value of Δ . It is seen in Fig. 4(b) that for $0.05 \lesssim \Delta/\lambda \lesssim 0.1$ (shown by green), x_Δ obtained from Eq. (19) is in good agreement with the analytical model. It is also seen that a small number of electrons can be pulled out from the plasma (see $\Delta \lesssim 0.05\lambda$, shown in yellow, in Fig. 4(b)).

However, the layer dynamics in PIC simulations doesn't fully obey theoretical assumptions. From Fig. 4(c) we can see that the layer is an average characteristic because single electrons constantly join and leave the layer. A typical electron lives in the layer one-two laser field periods and then enters the quasi-unperturbed plasma; it results in decrease of the layer energy compared to the theory (see \bar{x}_{PIC} on Fig. 3(c)) and modification of spatial distribution of energetic electrons (see \bar{x}_{PIC} on Fig. 4(c)). It alters the energetic properties of electrons and gamma-quanta in PIC compared to the theory.

B. Energetic properties and scaling laws

One of well-known features of many laser-plasma problems is that at relativistic laser intensities there is a similarity law²⁷: the interaction properties depend on the dimensionless parameter

$$S = \frac{n_e}{a_0 n_{cr}} = \frac{n_0}{a_0} \quad (20)$$

and not on n_0 and a_0 separately. The current model doesn't obey this scaling law strictly: equations (10-13) can't be reduced to a form with one dimensionless parameter even if radiation reaction is neglected (see also

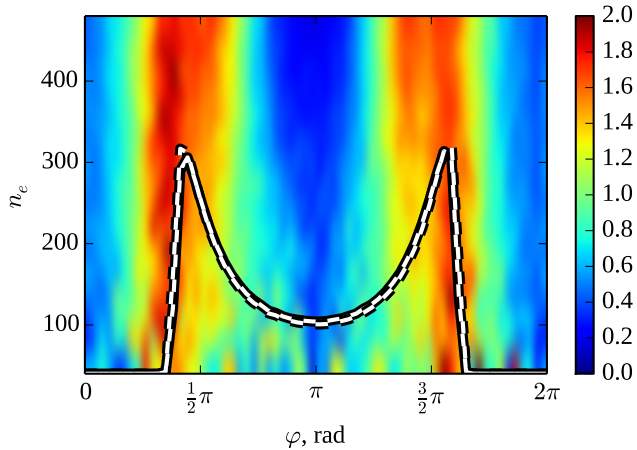


FIG. 5. Gamma-ray radiation pattern in PIC simulations at $a_0 = n_0$ ($S = 1$) varying from 40 to 480; lines show radiation pattern from the model for $S = 1$, $a_0 = 120$ (solid line), $a_0 = 240$ (dashed).

Sec. II A). However, the dependence on a_0 at $S = \text{const}$ is slight. We have compared radiation patterns from model and PIC simulations at different laser pulse intensities and foil densities but the same S parameters and the difference is negligible (see Fig. 5).

Figure 6(a) shows gamma-ray generation efficiency map in the $n_0 - a_0$ axis which is acquired from 144 PIC simulations; each point corresponds to the energy of gamma-rays generated during simulation timespan, normalized to the energy of the laser pulse. Different values of similarity parameter S correspond to sloping lines starting at the coordinate origin, it can be clearly seen from the figure that S determines different regimes of gamma-ray generation.

Higher a_0 values always result in increase of gamma-ray generation efficiency. The parameter region $S < 1$ (which is denoted as "I") corresponds to the relativistically self-induced transparency (RSIT) regime; the target becomes transparent because of the relativistic electron mass reduction and effective a_0 -times decrease of plasma frequency and increase of plasma density the electromagnetic waves can propagate through²⁸. Penetrating laser pulse produces extreme heating of electrons and ions in plasma and causes emission of hard photons due to ISE. In this region gamma-rays are generated most efficiently; however, the model is not applicable here because of RSIT and absence of the single electron layer being considered (we will discuss applicability conditions in more detail in the Sec. IV).

For $S \geq 1$, we can compare generation efficiency from PIC and model, the example of comparison under constant $S = 1$ and variable a_0 is shown in the 6(b). From the model, the efficiency is about one order less than from PIC simulations. However, the scaling corresponds to a power law of the approximately same degree in both cases that turns to be an important result. Possible reasons for

that: first, electrons in PIC simulations are not monoenergetic and have a certain Lorentz-factor distribution, so there is always a number of electrons that are hotter than the layer electrons in the model. Due to the radiation law $W \sim \gamma^4$, their contribution into the total energy output can essentially increase the gamma-ray generation power. Second, the model estimation for the number of electrons in the layer $n_e = n_0 x_\ell$ is obviously not true when layer disposition x_ℓ is about zero or even negative. In PIC simulations, the layer electrons sometimes had near-zero disposition, so model underestimates radiation of electrons in this part of trajectory.

IV. CONDITIONS OF APPLICABILITY

Based on 3D PIC simulations, we can distinguish a parameter region where the developed model can be applied. The main assumption of the model is that the incident laser pulse pushes the plasma electrons which form a single thin layer that reflects the laser pulse well so electrons behind the layer are almost unperturbed. We perform the analysis of electron Lorentz-factor distribution along longitudinal axis in different regimes (Fig. 7). It can be seen that the case of $S \sim 1$ corresponds to the model best. For $S < 1$, RSIT leads to effective propagation of the laser pulse through the target, and several electronic structures with high values of Lorentz-factor are formed across the target. For $S \gtrsim 2$, numerical simulations show that electron dynamics significantly differs from the case of $S \sim 1$ (where individual electrons stay in the layer up to several laser periods): the electrons generally escape the layer on each of laser half-periods, and new ('cold') electrons from the plasma replace them. Therefore electrons are grouped in thin bunches which propagate in x -direction (see Fig. 7, (c)). This effect leads to effective increase of overall electrons energy and decrease of gamma-rays generation efficiency because electrons in the layer do not reach high energies during laser half-period.

Therefore we define the region where the model can be applied as $1 \leq S < 2$. Limitation on a_0 parameter can be found from the requirement that we neglect quantum electrodynamical effects in this model so a_0 shouldn't be greater than ~ 500 . Obviously the laser pulse should be also strong enough so that the electron layer with high Lorentz-factor can be formed at all (thus $a_0 \gg 1$).

One should consider attainable plasma densities as well. For solid targets a typical electron density is in the order of $10^{22} - 10^{23} \text{ cm}^{-3}$ or higher so n_0 is in the order of hundreds (if $\lambda = 1 \mu\text{m}$). In order to achieve lower densities, some exotic targets are required.

The model also has the requirement of immobile ions. The numerical simulations that have been presented above are carried with immobile ions too, but several numerical experiments with moving ions were done. Charge-to-mass ratio of the ions was 0.25 of that for hydrogen atoms. The results (gamma-ray radiation pat-

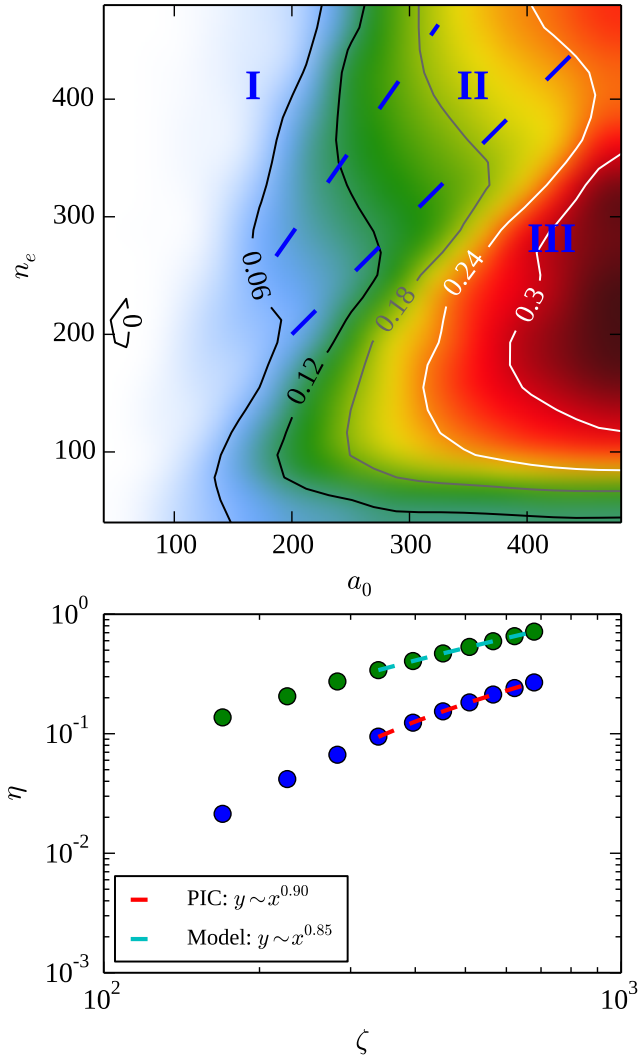


FIG. 6. (a) Gamma-ray generation efficiency map obtained from 144 PIC simulations. Foil thickness is $2\text{ }\mu\text{m}$, foil density and laser pulse intensity are variable parameters. II is the region where the model is applicable; III is the region of relativistically self-induced transparency (RSIT), in region I the stable electron layer is not formed in PIC. (b) Gamma-ray generation efficiency from PIC and analytical model at $S = 1$ ($a_0 = n_0$).

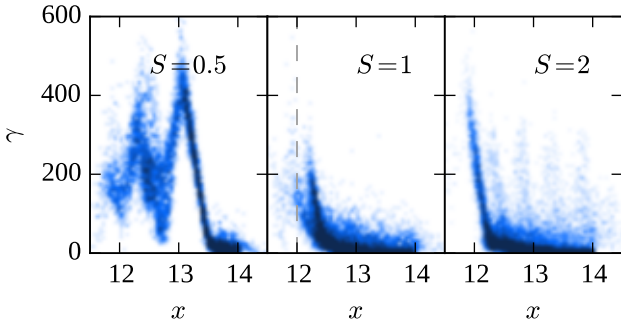


FIG. 7. Electron Lorentz-factor distribution along x -axis at $t = 5.8\lambda/c$ (laser pulse is incident from the left) for different values of S . Only electrons from the region near the x axis, where laser pulse front is plane, are shown.

tern, electron layer dynamics) didn't change drastically in case of moving ions, although gamma-ray generation efficiency became lower about 2 times. To get mostly aligned with the model and improve gamma-ray generation efficiency, one should take as smallest ion charge-to-mass ratio as possible.

V. CONCLUSION

The self-consistent model that describes electron dynamics in the interaction of a relativistically strong laser field with overdense plasma halfspace is presented. Plasma electrons are pushed by $\mathbf{v} \times \mathbf{B}$ force and form a thin layer on the plasma edge. This layer coherently emit electromagnetic spikes as the laser pulse reflection and considerably suppress the fields transmitted into the plasma. The back-reaction of the coherently emitted fields is taken into account, as well as radiation reaction caused by the incoherent emission of the layer.

The back-reflected field presents a train of electromagnetic spikes emitted when the electron layer has maximal velocity towards the laser pulse. These time instances correspond to the minimal value of the electron Lorentz factor that means not optimal conditions of short-spike generation and low value of the cut-off in the spectrum of the reflected field^{17,18}.

When electrons are ultrarelativistic, the supposition that the plasma dynamics is governed by the only parameter $S = n_0/a_0$ (not by n_0 and a_0 separately) is often used^{13,17,27}. It yields the electron Lorentz factor $\gamma \propto a_0$. But the presented theory demonstrates that the process of electron acceleration can be a fine effect. Namely, it occurs that $d\gamma/dt = 0$ if we neglect the electron rest mass and fields behind the layer in the framework of the presented theory¹³. The accurate analysis shows that the equation for the electron energy depends on two parameters n_0 and a_0 separately, and yields that the ratio γ/a_0 drops with the increase of a_0 . The losses caused by the incoherent photon emission strengthen this drop.

The presented model allows one to find electron trajectories (including Lorentz factors) and, hence, incoherent synchrotron emission from the plasma edge. Plasma edge dynamics and gamma-ray radiation pattern are in a fairly good agreement with the results of 3D PIC simulations. Namely, the model predicts a two-lobe radiation pattern with lobes approximately parallel to the electric field direction of the incident laser pulse. This radiation pattern is caused by the 8-like electron trajectories extended along this direction. It is also predicted that for $S \approx 1$, in contrast to the electron re-injection regime¹², emission towards the incident laser pulse is much weaker than in perpendicular direction, that is also in good agreement with 3D PIC simulations. Therefore, angular distribution of gamma-rays can specify the laser-plasma interaction regime in experiments at ultrahigh intensity.

PIC simulations reveal that a thin electron layer is formed on the plasma edge if $S = n_0/a_0 \approx 1$. In the case

of $S \lesssim 1/2$ relativistically self-induced transparency occurs, and the laser pulse propagates through the plasma. If $S \gtrsim 2$, the skin depth (the thickness of the current distribution in the plasma) becomes larger than electron displacement perpendicular to the plasma surface, and a lot of electrons escapes to the plasma bulk. If the laser pulse duration or the laser pulse magnitude a_0 is high, ion motion becomes considerable. This case is also beyond the region where the model is applicable.

From numerical simulations we also see that individual electrons stay near the plasma edge generally a half of the laser period, thus, electrons permanently leave and join the layer. Electrons that leave the layer transfer the laser energy into the plasma bulk and heat the target. Electrons that join the layer have energy which is significantly different from the average electron energy in the layer that may cause a sizable discrepancy between model predictions and PIC results. Namely, PIC and the model gives different values for overall electron energy and generation efficiency of gamma rays. Nevertheless, the analytical model yields the same scaling of the generation efficiency as PIC if $S \approx 1$.

Therefore, the presented theoretical model can be used for the analysis of coherent and incoherent photon emission for $n_0 \sim a_0$. The model can be used for optimization of high harmonic and gamma-ray generation in the interaction of ultraintense laser pulses with plasmas. Some results of this work would be extended to the case of obliquely incident laser pulses.

VI. ACKNOWLEDGEMENTS

Numerical simulations were carried out on the computer cluster of the Laboratory of Supercomputer Technologies in Non-Linear Optics, Plasma Physics and Astrophysics in University of Nizhny Novgorod.

This work has been supported by the Government of the Russian Federation (Project No. 14.B25.31.0008) and by the Russian Foundation for Basic Research (Grant No. 15-02-06079).

¹Y. Glinec, J. Faure, L. L. Dain, S. Darbon, T. Hosokai, J. J. Santos, E. Lefebvre, J. P. Rousseau, F. Burgy, B. Mercier, and V. Malka, Physical Review Letters **94**, 025003 (2005).

²S. Cipiccia, S. M. Wiggins, R. P. Shanks, M. R. Islam, G. Vieux, R. C. Issac, E. Brunetti, B. Ersfeld, G. H. Welsh, M. P. Anania, D. Maneuski, N. R. C. Lemos, R. A. Bendoyro, P. P. Rajeev, P. Foster, N. Bourgeois, T. P. A. Ibbotson, P. A. Walker, V. O. Shea, J. M. Dias, and D. A. Jaroszynski, Journal of Applied Physics **111**, 3302 (2012).

³K. Ta Phuoc, S. Corde, C. Thaury, V. Malka, A. Tafzi, J. P. Goddet, R. C. Shah, S. Sebban, and A. Rousse, Nature Photonics, Volume 6, Issue 5, pp. 308-311 (2012). **6**, 308 (2012).

⁴L. A. Gizzi, M. P. Anania, G. Gatti, D. Giulietti, G. Grittani, M. Kando, M. Krus, L. Labate, T. Levato, Y. Oishi, and F. Rossi, Nuclear Instruments and Methods in Physics Research Section B: Beam Interactions with Materials and Atoms **309**, 202 (2013).

⁵S. Chen, N. D. Powers, I. Ghebregziabher, C. M. Maharjan, C. Liu, G. Golovin, S. Banerjee, J. Zhang, N. Cunningham,

A. Moorti, S. Clarke, S. Pozzi, and D. P. Umstadter, Physical Review Letters **110**, 155003 (2013).

⁶N. D. Powers, I. Ghebregziabher, G. Golovin, C. Liu, S. Chen, S. Banerjee, J. Zhang, and D. P. Umstadter, Nature Photonics **8**, 28 (2014).

⁷G. Sarri, D. J. Corvan, W. Schumaker, J. M. Cole, A. Di Piazza, H. Ahmed, C. Harvey, C. H. Keitel, K. Krushelnick, S. P. D. Mangles, Z. Najmudin, D. Symes, A. G. R. Thomas, M. Yeung, Z. Zhao, and M. Zepf, Physical Review Letters **113**, 224801 (2014).

⁸S. Cipiccia, M. R. Islam, B. Ersfeld, R. P. Shanks, E. Brunetti, G. Vieux, X. Yang, R. C. Issac, S. M. Wiggins, G. H. Welsh, M. P. Anania, D. Maneuski, R. Montgomery, G. Smith, M. Hoek, D. J. Hamilton, N. R. C. Lemos, D. Symes, P. P. Rajeev, V. O. Shea, J. M. Dias, and D. A. Jaroszynski, Nature Physics **7**, 867 (2011).

⁹L. M. Chen, W. C. Yan, D. Z. Li, Z. D. Hu, L. Zhang, W. M. Wang, N. Hafz, J. Y. Mao, K. Huang, Y. Ma, J. R. Zhao, J. L. Ma, Y. T. Li, X. Lu, Z. M. Sheng, Z. Y. Wei, J. Gao, and J. Zhang, Nature Scientific Reports **3**, 1912 (2013).

¹⁰I. A. Andriyash, R. Lehe, A. Lifschitz, C. Thaury, J.-M. Rax, K. Krushelnick, and V. Malka, Nature Communications **5**, 4736 (2014).

¹¹T. Nakamura, J. K. Koga, T. Z. Esirkepov, M. Kando, G. Korn, and S. V. Bulanov, Phys. Rev. Lett. **108**, 195001 (2012).

¹²C. S. Brady, C. P. Ridgers, T. D. Arber, A. R. Bell, and J. G. Kirk, Phys. Rev. Lett. **109**, 245006 (2012).

¹³E. N. Nerush, I. Y. Kostyukov, L. Ji, and A. Pukhov, Physics of Plasmas **21**, 013109 (2014).

¹⁴C. P. Ridgers, C. S. Brady, R. Duclous, J. G. Kirk, K. Bennett, T. D. Arber, A. P. L. Robinson, and A. R. Bell, Phys. Rev. Lett. **108**, 165006 (2012).

¹⁵L. L. Ji, A. Pukhov, E. N. Nerush, I. Y. Kostyukov, B. F. Shen, and K. U. Akli, Physics of Plasmas **21**, 023109 (2014), 10.1063/1.4866014.

¹⁶C. S. Brady, C. P. Ridgers, T. D. Arber, and A. R. Bell, Physics of Plasmas **21**, 033108 (2014).

¹⁷A. A. Gonoskov, A. V. Korzhimanov, A. V. Kim, M. Marklund, and A. M. Sergeev, Phys. Rev. E **84**, 046403 (2011).

¹⁸D. An der Brügge and A. Pukhov, Physics of Plasmas **17**, 3110 (2010).

¹⁹B. Dromey, S. Rykovanov, M. Yeung, R. Hörlein, D. Jung, D. C. Gautier, T. Dzelzainis, D. Kiefer, S. Palaniyppan, R. Shah, J. Schreiber, H. Ruhl, J. C. Fernandez, C. L. S. Lewis, M. Zepf, and B. M. Hegelich, Nature Physics, Volume 8, Issue 11, pp. 804-808 (2012). **8**, 804 (2012).

²⁰S. G. Rykovanov, H. Ruhl, J. Meyer-ter Vehn, R. Hörlein, B. Dromey, M. Zepf, and G. D. Tsakiris, New Journal of Physics **13**, 023008 (2011).

²¹S. V. Bulanov, T. Z. Esirkepov, M. Kando, S. S. Bulanov, S. G. Rykovanov, and F. Pegoraro, Physics of Plasmas, Volume 20, Issue 12, article id. 123114 13 pp. (2013). **20**, 123114 (2013).

²²C. P. Ridgers, C. S. Brady, R. Duclous, J. G. Kirk, K. Bennett, T. D. Arber, and A. R. Bell, Physics of Plasmas **20**, 056701 (2013).

²³M. Tamburini, T. V. Liseykina, F. Pegoraro, and A. Macchi, Physical Review E **85**, 016407 (2012).

²⁴M. Chen, A. Pukhov, T.-P. Yu, and Z.-M. Sheng, Plasma Physics and Controlled Fusion **53**, 014004 (2011).

²⁵R. Capdessus, E. d'Humières, and V. T. Tikhonchuk, Physical Review E **86**, 036401 (2012).

²⁶L. D. Landau and E. M. Lifshitz, *The Classical Theory of Fields* (Elsevier, Oxford, 1975).

²⁷S. Gordienko and A. Pukhov, Physics of Plasmas **12**, 043109 (2005).

²⁸P. Kaw and J. Dawson, Physics of Fluids (1958-1988) **13**, 472 (1970).